



# Analysis of Thermal and Flow Characteristics in a Combined Cross-Flow and Jet-Flow Configuration with Flow-Guiding Fins

M. S. Ozturk<sup>1</sup> and T. Demircan<sup>2†</sup>

<sup>1</sup> Department of Mechanical Engineering, Graduate School of Natural and Applied Sciences, Kirikkale University, 71450, Kirikkale, Turkey

<sup>2</sup> Department of Mechanical Engineering, Faculty of Engineering and Architecture, Kirikkale University, 71450, Kirikkale, Turkey

†Corresponding Author Email: [tolgademircan@kku.edu.tr](mailto:tolgademircan@kku.edu.tr)

(Received March 21, 2022; accepted June 11, 2022)

## ABSTRACT

This study investigated the enhanced cooling of electronic components at high temperatures with cross-flow and jet-flow combinations. The cooling performance of four different model geometries (Models 1, 2, 3, and 4) of an electronic component was analysed by considering different jet-to-channel inlet velocity ratios ( $V_j/V_c$ ) and ratios of the distance between the jet and impinging surface to jet diameter ( $H/D$ ). The  $V_j/V_c$  and  $H/D$  ratios were varied in the 0–3 and 2–4 ranges, respectively, in the computational fluid dynamics analysis. The thermal and flow characteristics were revealed through a comparative result analysis, also considering results from the literature. The heat transfer improved, the Nusselt number increased, and the electronic surface temperature decreased with an increase in the  $V_j/V_c$  ratio. However, the Nusselt number decreased with an increase in the  $H/D$  ratio. Models 2 and 4 had higher heat transfer from the electronic component than the other models. A low  $H/D$  ratio and low  $V_j/V_c$  ratio yielded higher heat transfer in Model 3 than in Model 1.

**Keywords:** Cross-flow; Impinging jet; Electronic cooling; Heat transfer; CFD.

## NOMENCLATURE

$A_c$	cross-sectional area of the channel	$q''$	heat flux
$D$	nozzle diameter	$Re_j$	jet Reynolds numbers
$D_{hc}$	channel hydraulic diameter	$Re_c$	channel Reynolds numbers
$H$	channel height (Distance between the jet and impinging surface)	$T_j$	jet inlet temperature
$h$	length of one side of the electronic component	$T_c$	channel inlet temperature
$h$	heat transfer coefficient	$T_w$	surface temperature of electronic component
$H/D$	ratio of the distance between the jet and impinging surface to jet diameter	$u$	velocity component in the $x$ -direction
$k$	turbulent kinetic energy	$v$	velocity component in the $y$ -direction
$k_a$	thermal conductivity of air	$V_j$	jet inlet velocity
$L$	length of the channel	$V_c$	channel inlet velocity
$Nu_x$	local Nusselt number	$V_j/V_c$	jet-to-channel inlet velocity ratio
$\overline{Nu}_A$	average Nusselt number	$W$	channel width
$P_{out}$	channel outlet pressure	$\rho$	density of air
$P_{atm}$	atmospheric pressure	$\alpha$	fin angle
$P_c$	wetted perimeter of the cross-section	$\varepsilon$	dissipation rate of kinetic energy
$Pr$	Prandtl number	$\mu$	dynamic viscosity of air

## 1. INTRODUCTION

Electronic systems currently have wide applications in various sectors, including transportation, health, space, and the military. Electronic systems contain numerous circuits comprising several electronic components. When the system operates, the electronic components generate heat, leading to high temperatures. For safe and stable system operation, electronic components that reach high temperatures must be cooled and maintained at safe operating temperatures. Various cooling methods are currently employed to cool the electronic circuit components. The most preferred method is to supply a low-temperature fluid to the entire circuit and cool the entire electronic components in the circuit by forced convection. All electronic components can be cooled to a certain extent using this technique. However, if the circuit has a component at an extremely high temperature, adequate to reduce the component temperature to the safe limit might be difficult. Another cooling technique involves using an impinging jet flow. This method is based on the high-speed impingement of a low-temperature fluid on the high-temperature electronic component. Although an impinging jet can locally cool the high-temperature circuit component, this method might not cool the other circuit components.

In this study, a hybrid cooling method that uses the advantages of both cooling methods and minimises their disadvantages is considered. For this purpose, a combination of cross-flow and impinging jet is proposed for the cooling of electronic circuit components. This hybrid cooling system facilitates a common flow by cross-flow and impinging jet-flow inside the control volume for effective cooling of the electronic circuit components.

The literature has numerous experimental and numerical studies on cross-flow and impinging jet flow. The majority of these studies focus on the heat transfer effects of parameters such as the flow area geometry, turbulence model, Reynolds number, nozzle cross-section, distance between the nozzle and impinging surface, and electronic component heat flux. However, only a few studies have investigated a cross-flow and impinging jet-flow hybrid model, as discussed below.

Choo *et al.* (2012) experimentally investigated the thermal characteristics of inclined impinging jets. The distance between the jet and plate significantly affected the heat transfer. The impingement point and average Nusselt number increased when the inclination angle increased for small jet placement distances. The impingement point and average Nusselt number decreased when the inclination angle increased for large jet placement distances. Hadipour and Zargarabadi (2018) experimentally and numerically investigated a circular jet impinging on a concave surface. The heat transfer increased as the jet diameter increased at a constant Reynolds number. The heat transfer was enhanced at small jet-to-plate distances. Kuraan *et al.* (2017) experimentally analysed the thermal and flow characteristics of a circular water jet impinging

vertically on a flat plate for small nozzle-to-plate distances. The normalised stagnation Nusselt number and hydraulic jump diameter in the jet deflection region was inversely proportional to the nozzle-to-plate spacing. San and Chen (2014) experimentally investigated the effects of five circular jets vertically impinging on a flat plate with a constant heat flux on heat transfer. The jet interaction at the impinging plate decreased as jet-to-jet spacing to jet diameter ratio ( $S/D$ ) and jet height to jet diameter ratio ( $H/D$ ) increased. Increasing the  $S/D$  ratio from 2 to 8 increased the Nusselt number by 7% to 45%. Kilic and Ali (2019) numerically investigated the impact of nanofluid use in multiple impinging jets considering CuO–water,  $Al_2O_3$ –water, Cu–water and TiO–water nanofluids. The increase in the nanoparticle volume ratio increased the average Nusselt number by approximately 10.4%. The increase in heat flux had no significant effect on the average Nusselt number.

Wongcharee *et al.* (2017) experimentally investigated the effect of swirling flow on the heat transfer during cooling with an impinging jet. The study used water and CuO nanofluid with variable nanoparticle concentrations as the cooling fluid. The Nusselt number decreased as the  $H/D$  ratio increased. Compared with pure water, the nanofluids with 2.0% and 3.0% nanoparticle concentrations resulted in higher heat transfer. Xiao *et al.* (2011) numerically investigated the hydrodynamic behaviour of a single jet and four tandem jets inside a cross-flow for different Reynolds numbers and jet-to-cross-flow velocity ratios. The study analysed the effect of the jet-to-cross-flow velocity ratio on the flow structure. Jing *et al.* (2018) numerically analysed the cooling performance of an impinging jet for three different target shapes (straight, concave, and V-shaped) and various surface layouts (sparse dent/bulge, dense dent/bulge, and triangle-ribbed dent/bulge). The Nusselt number was not affected by the sparse and dense layouts. The heat transfer performance was high for dent/bulge layout for irregular channels with low friction. Zhu *et al.* (2018) numerically analysed the transient heat transfer properties and cooling velocity for a series of air jets placed vertically on a high-temperature straight plate with small jet-to-plate distances. The reverse-flow jets significantly increased heat transfer. As the  $S/D$  ratio increased, the damping duration decreased.

Ali (2021) experimentally investigated the use of phase change material incorporating nanoparticles for passive cooling of electronic components. The heat sink assisted with nanoparticle incorporated phase change material and heat pipe had excellent heat transfer performance for low heating loads. Ingole and Sundaramb (2016) experimentally investigated the cooling performance of an inclined air jet impinging on a straight surface. The average Nusselt number decreased as  $H$  increased. Furthermore, the variation in the Nusselt number with the jet inclination angle was identified. The 45° and 60° inclination angles yielded better cooling performance than the 15° and 75° inclination angles. Ghaneifar *et al.* (2021) numerically investigated the mixed convection of  $Al_2O_3$  nanofluid in a horizontal

channel with two heat sources at the centre. The study investigated the effects of different parameters, such as geometry, Richardson number, Reynolds number, and thermal conductivity, on heat transfer. [Hatamia et al. \(2018\)](#) numerically and experimentally investigated the confined and unconfined impinging synthetic jets to improve the cooling performance. The Nusselt number increased with an increase in Reynolds number, and the maximum heat transfer occurred at  $H/D = 4$ . The authors observed that the heat transfer rate of the unconfined synthetic jet was approximately 30% higher than that of the confined synthetic jet. [Yu et al. \(2017\)](#) numerically analysed the heat transfer characteristics of a circular jet impinging on a high-temperature straight plate. An increase in the  $H/D$  ratio decreased the cooling time.

[Khan et al. \(2022\)](#) reviewed the experimental, numerical, and analytical studies on micro- and mini-channels used for electronic component cooling, considering the nanofluid thermophysical properties, porous heat sinks, and nanofluid usage details. [Selimefendigil and Öztop \(2014\)](#) numerically analysed the cooling of a heated horizontal surface with a rectangular jet using  $Al_2O_3$  as the nanofluid. The heat transfer increased as the Reynolds number and nanoparticle concentration increased. The Nusselt number at the stagnation point generally increased with increasing frequency. [Zhong et al. \(2019\)](#) studied the flow and heat transfer characteristics of inclined jets inside a cross-flow using the large eddy simulation method. The jet inclination angle was set to  $35^\circ$ . The heat-transfer coefficient was affected by the time-averaged transportation terms. [Sun et al. \(2016\)](#) experimentally analysed the variation in the impinging jet cooling performance for different nanoparticle concentrations, jet diameters, and jet lengths. The nanofluid use significantly affected heat transfer. An increase in the nanoparticle concentration increased the heat transfer. [Arshad and Ali \(2017\)](#) experimentally investigated the pressure drop and heat transfer in straight mini-channels using  $TiO_2$  nanofluid. The pressure increased with a decrease in the heating power. The thermal performance of the nanofluid increased by approximately 12.75% with a decrease in the heating power.

[Masip et al. \(2020\)](#) experimentally investigated the cooling of an electronic component inside a channel using a cross-flow and impinging jet combination. The experiments were conducted for different channel Reynolds numbers and jet-to-channel Reynolds number ratios. Cooling with the jet-cross-flow combination showed higher performance than cooling with only cross-flow. [Guoneng et al. \(2014\)](#) investigated the heat transfer performance of an impinging jet in a cross-flow. The study considered the jet-to-cross-flow mass ratio, Reynolds number, and jet diameter in the ranges of 2%–8%, 1434–5735, and 2–4 mm, respectively. The impinging jet significantly enhanced heat transfer. An increase in the jet-to-cross-flow mass ratio and Reynolds number increased heat transfer. However, heat transfer decreased as the jet diameter increased.

[Guoneng et al. \(2016\)](#) experimentally investigated the convective heat transfer in a flow consisting of cross-flow and multiple jets. The convective heat transfer was significantly increased using multiple jets. The authors developed an empirical correlation with 17.2% uncertainty using the experimental data. [Masip et al. \(2012\)](#) experimentally investigated the combination of jet flow and axial flow applied to a cube representing an electronic component. The channel Reynolds number was varied in the 3410–8880 range. The experiments were conducted for channel-to-jet Reynolds number ratios of 0.5, 1.0, and 1.5. The Reynolds number ratio affected the drag produced on the jet and the deviation of the jet from its geometric axis.

[Wang et al. \(2015\)](#) experimentally investigated the vortex generator pair (VGP) usage for a jet flow applied in cross-flow. The heat transfer on the target surface was significantly increased by adding a VGP to the flow geometry. Heat transfer was optimum when the distance between the jet nozzle and vortex generator was  $4D$ . [Wang et al. \(2016\)](#) experimentally investigated the effects of vortex generators on heat transfer in jet-flow-cross-flow applications. The jet Reynolds number was 15000. The cross-flow Reynolds number varied between 40000 and 64000. The VGP significantly increased the heat transfer. The Reynolds number, VGP shape, and VGP height affected heat transfer. [Demircan and Türkoğlu \(2010\)](#) numerically investigated the effects of an oscillating air jet applied to a straight surface on the heat transfer and flow structure. The Nusselt number increased with an increase in the Reynolds number. Heat transfer increased as the oscillation frequency increased. [Wang et al. \(2019\)](#) experimentally investigated the effect of a vortex generator on heat transfer for cross-flow/jet-flow applications. Accordingly, the jet speed was maintained at 12 m/s, and the cross-flow speed varied between 5–8 m/s. The presence of the vortex generator increased the heat transfer. [Mohammadshahi et al. \(2021\)](#) experimentally investigated the flow characteristics and heat transfer of an oscillating jet in a cross-flow. The heat transfer was dominated by cross-flow, and the change in the jet-flow blowing ratio had no significant impact on the heat transfer. The cross-flow and jet-flow use increased the heat transfer two-fold compared with cross-flow and oscillating jet-flow use.

[Saleha et al. \(2015\)](#) numerically investigated an impinging jet in a cross-flow configuration for cooling an electronic component considering different chamfer heights and Reynolds numbers. A suitable chamfer height improved the cooling performance. The highest heat transfer was for a jet-flow-to-cross-flow Reynolds number ratio of 1.5 and 4 mm chamfer height. [Mergen \(2014\)](#) numerically analysed the cooling of an electronic component with a constant heat flux using an impinging jet in cross-flow. The study considered duct Reynolds number of 2000–8000, jet Reynolds number of 10000–25000 and  $H/D$  value of 1.5–2. When the jet-to-duct Reynolds number ratio decreased, the surface temperature of the electronic component increased, leading to deterioration in heat transfer. [Larraona et](#)

*al.* (2013) numerically analysed cooling by an impinging-jet and cross-flow combination (IJCF) for an electronic component with constant heat flux. The average Nusselt number was inversely proportional to the height of the electronic component and directly proportional to the duct Reynolds number and velocity ratio. An increased duct Reynolds number, jet diameter, and velocity ratio caused an increase in the pressure loss. Using IJCF yielded a higher cooling efficiency than using only cross-flow (CF).

Örs (2017) numerically analysed the cooling of an electronic component inside a duct with a constant surface temperature using an impinging-jet and cross-flow combination. The study analysed the effect of different chamfer heights and Reynolds numbers on heat transfer. An increased chamfer height and jet Reynolds number significantly increased the heat transfer from the electronic component. Demircan (2019) numerically analysed the cooling of an electronic circuit component with cross-flow and jet combinations. The study analysed different jet-to-channel inlet velocity ratio ( $V_j/V_c$ ) values in the 30000–90000 Reynolds number (based on duct inlet velocity) range. The heat transfer increased significantly with an increase in Reynolds number and  $V_j/V_c$  ratio. Maghrabie *et al.* (2017) numerically investigated the cooling of a system comprising seven electronic components in a duct using CF and IJCF. The study analysed seven different jet positions and jet-to-channel Reynolds number ratios of 1, 2, and 4. The IJCF provided better cooling than the CF for four jet positions.

Thus, the various studies reported in the literature focused on impinging-jets or cross-flows separately. A few recent studies have studied the IJCF. These studies have majorly focused on the effects of variations in channel and jet inlet velocities, as well as variations in duct height or jet diameter, on heat transfer. Unlike previous studies, this study investigated the effects of multiple parameters on flow and heat transfer. The impact of the jet-to-channel inlet velocity ratio ( $V_j/V_c$ ), channel height to jet-diameter ratio ( $H/D$ ), and the addition of flow-guiding fin to the geometry were considered. An analysis was conducted for four model geometries, four  $V_j/V_c$  ratios, and three  $H/D$  ratios to investigate the heat transfer from an electronic component at the centre of a rectangular channel with constant heat flux. Using the results obtained from the analyses, the effects of variations in the  $V_j/V_c$  and  $H/D$  ratios on the flow and thermal characteristics were analysed.

## 2. PROBLEM DEFINITION AND MATHEMATICAL FORMULATION

The study considered the cooling of an electronic component with a cross-flow and an impinging jet. An electronic component with constant heat flux positioned at the base of a channel of a rectangular cross-section was analysed. The air supplied at a constant velocity  $V_c$  from the channel inlet created a primary flow over the electronic component to cool the component. In addition, a secondary air flow with

constant velocity  $V_j$  from a circular nozzle above the electronic component was directed to the top surface of the electronic component. When these two flows impinged on the electronic component, a complex flow structure developed around it. Four different model geometries were developed to analyse the flow and heat transfer characteristics around the electronic components in detail. A schematic of the model geometry is presented in Fig. 1.

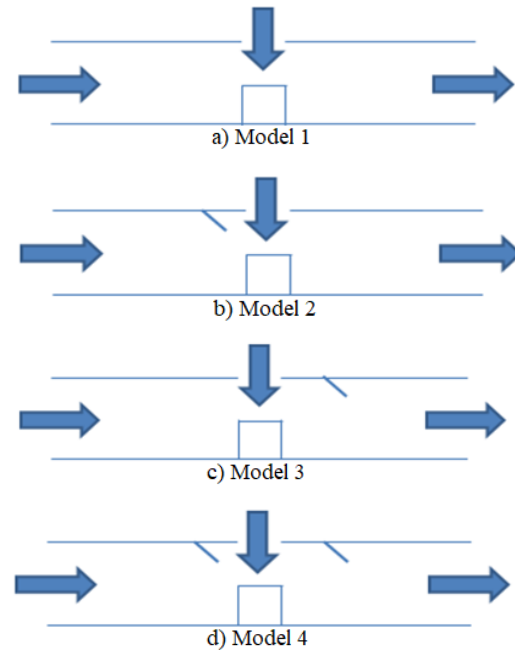


**Fig. 1. Schematic representation of the models; a) Model 1, b) Model 2, c) Model 3, and d) Model 4.**

As shown in Fig. 1, the model geometries were similar. The detailed geometry of Model 4 is shown in Fig. 2. The dimensions of the models investigated in this study were fixed based on a similar study by Saleha *et al.* (2015). The nozzle diameter was  $D=15$  mm, and all other dimensions were determined based on  $D$ . The channel length was  $L=66D$ , height was  $H=2D, 3D,$  or  $4D$ , and width was  $W=4D$ . The electronic component was cubic with edge length  $h=4D/3$ . The flow-guiding fin length was  $h_f=D$ , the distance between the fin and jet was  $x=D$ , and the fin width was  $t=D/7.5$ . The jet diameter  $D$ , channel height  $H$ , channel length  $L$ , channel width  $W$ , shape of the electronic component (cube), edge length  $h$ , fin length, fin width, fin angle, and distance between the jet and fin were constant for all models.

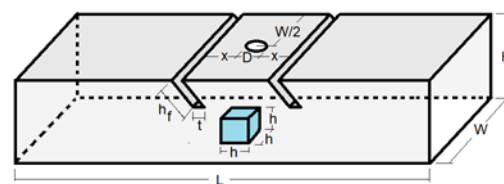


**Fig. 2. Schematic of Model 4.**

## 2.1 Governing Differential Equations

To numerically analyse the flow and heat transfer characteristics, the continuity, momentum, energy, and turbulence equations must be solved using suitable boundary conditions. The time-independent, incompressible, three-dimensional governing differential equations used in this study (Saleha *et al.* 2015, Mergen 2014, Örs 2017, Zuckerman and Lior 2006) are given below.

**Continuity equation:**

$$\frac{\partial \bar{u}_i}{\partial x_j} = 0 \quad (1)$$

**Momentum equation:**

$$\rho \frac{\partial}{\partial x_j} (\bar{u}_i \bar{u}_j) = -\frac{\partial \bar{p}}{\partial x_i} + \frac{\partial}{\partial x_j} \left[ \mu \left( \frac{\partial \bar{u}_i}{\partial x_j} + \frac{\partial \bar{u}_j}{\partial x_i} \right) - \rho \overline{u'_i u'_j} \right] \quad (2)$$

**Energy equation:**

$$\rho C_p \frac{\partial}{\partial x_i} (\bar{u}_i \bar{T}) = \frac{\partial}{\partial x_i} \left[ k \frac{\partial \bar{T}}{\partial x_i} - \rho C_p \overline{T' u'_i} \right] \quad (3)$$

**Turbulent kinetic energy:**

$$\frac{\partial}{\partial x_i} (\rho k u_i) + \frac{\partial}{\partial y} (\rho k) = \frac{\partial}{\partial x_j} \left[ \left( \mu + \frac{\mu_t}{\sigma_k} \right) \frac{\partial k}{\partial x_j} \right] - \rho \overline{u'_i u'_j} \frac{\partial u_j}{\partial x_i} - \rho \varepsilon \quad (4)$$

**Dissipation rate of kinetic energy:**

$$\frac{\partial}{\partial x_i} (\rho \varepsilon u_i) + \frac{\partial}{\partial y} (\rho \varepsilon) = \frac{\partial}{\partial x_j} \left[ \left( \mu + \frac{\mu_t}{\sigma_\varepsilon} \right) \frac{\partial \varepsilon}{\partial x_j} \right] + C_{1\varepsilon} \frac{\varepsilon}{k} G_k - C_{2\varepsilon} \rho \frac{\varepsilon^2}{k} \quad (5)$$

$$\mu_t = C_\mu \rho \frac{k^2}{\varepsilon} \quad (6)$$

In these equations,  $\sigma_k = 1$ ,  $C_{1\varepsilon} = 1.44$ ,  $C_{2\varepsilon} = 1.92$ , and  $C = 0.09$ , according to Mergen 2014;  $\sigma_k = 1$ ,  $C_{1\varepsilon} = 1.44$ ,  $C_{2\varepsilon} = 1.92$ , and  $C_\mu = 0.09$ , according to Örs 2017;  $\sigma_\varepsilon = 1.3$  (Mergen 2014, Örs 2017).

## 2.2 Boundary Conditions

Air was supplied from the nozzle inlet at velocity  $V_j$  and temperature  $T_j = 20$  °C vertically to the top surface of the electronic component. The air at the channel entrance was at constant velocity  $V_c = 2.94$  m/s and temperature  $T_c = 20$  °C; the velocity at the channel entrance only had a horizontal component ( $u = V_c$ ). The channel outlet was open to the atmosphere. Therefore, the channel outlet pressure was assumed to be equal to the atmospheric pressure ( $P_{out} = P_{atm}$ ). The temperature difference at the outlet of the channel was assumed to be negligible, and  $\partial T / \partial x = 0$  at the outlet. The no-slip condition was assumed at the walls of the channel and electronic component, and all velocity component values were zero at the walls. All channel walls were assumed to be insulated ( $\partial T / \partial x = 0$ ). For the electronic component surfaces, a constant of 3000 W/m<sup>2</sup> was assumed, in line with other studies in the literature

(Mergen 2014, Ravanji and Zargarabadi 2020, Köseoğlu 2007).

## 2.3 Other Equations

The following equations were used to calculate the Nusselt number, Reynolds number, and convection heat transfer to analyse the results obtained in this study.

**Heat transfer coefficient:** (Demircan 2019, Incropera *et al.* 2007)

$$h = \frac{\dot{q}''}{T_w - T_b} = - \left. \frac{k}{(T_w - T_b)} \frac{\partial T}{\partial n} \right|_{n=0} \quad (7)$$

Local Nusselt number: (Ingle and Sundaram 2016, Mergen 2014, Larraona *et al.* 2013, Örs 2017, Demircan 2019, Maghrabie *et al.* 2017)

$$Nu_x = \frac{h D_h}{k} = - \left. \frac{D_h}{(T_w - T_b)} \frac{\partial T}{\partial n} \right|_{n=0} \quad (8)$$

**Average Nusselt number** (Demircan, 2019)

$$\overline{Nu}_A = \frac{1}{A} \int_A Nu_x dA \quad (9)$$

**Channel hydraulic diameter:**

The hydraulic diameter of the channel was calculated using Eq. (10) (Mergen 2014, Örs 2017, Maghrabie *et al.* 2017, Incropera *et al.* 2007), where  $A_c$  is the cross-sectional area of the channel,  $P_c$  is the wetted perimeter of the cross-section of the channel,  $H$  is the channel height, and  $W$  is the channel width.

$$D_{hc} = \frac{4A_c}{P_c} \quad (10)$$

$$A_c = (H)(W) \quad (11)$$

$$P_c = 2(H + W) \quad (12)$$

**Reynolds number:**

The channel and jet Reynolds numbers were calculated using channel hydraulic diameter and jet diameter, respectively, as the characteristic lengths. The channel and jet Reynolds number calculations are given by Eqs. (12) and Eq. (13), respectively (Incropera *et al.* 2007).

$$Re_j = \frac{\rho V_j D_j}{\mu} \quad (13)$$

$$Re_c = \frac{\rho V_c D_{hc}}{\mu} \quad (14)$$

## 3. NUMERICAL SOLUTION

The continuity, moment, energy, and turbulence equations, which are the governing differential equations in this study, were numerically solved using the boundary conditions. For this purpose, Fluent software based on computational fluid dynamics was used. The realisable  $k$ - $\varepsilon$  turbulence model was used. The discretisation followed the second-order upwind scheme for energy and momentum equations and the first-order upwind scheme for turbulence equations.

### 3.1 Mesh Structure

The computational domain was divided into control volumes to create a mesh structure. A sparse mesh was used in the regions where the gradients of parameters such as velocity and temperature were low (channel interior), and a fine mesh was used in the regions where the gradients of the parameters were high (channel surfaces, fin surfaces, and the surroundings of the electronic component). To maintain the first grid layer within the viscous boundary layer, the mesh element size for a  $y^+$  value of approximately 1 was calculated. In this context, the element size of the mesh adjacent to the electronic component surfaces was selected to be 0.075 mm. The mesh structure for Model 4 geometry is shown in Fig. 3 as an example.

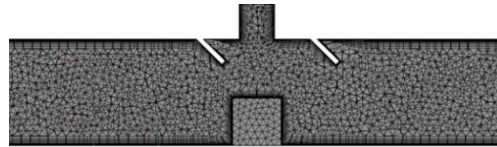


Fig. 3. Mesh structure for Model 4.

### 3.3 Convergence Control

For convergence of the numerical solutions, the convergence criteria were selected as  $10^{-3}$  for the momentum and turbulence equations and  $10^{-6}$  for the energy equation. Additionally, the inlet and outlet mass flows inside the solution volume were compared, and the net mass flow loss was less than  $10^{-7}$ .

### 3.2 Mesh Independence Test

In this study, an analysis of different mesh structures was conducted to ensure that the solution was independent of the grids. Three optimum mesh structures were selected for the three  $H/D$  ratios. The optimum mesh had approximately 586000, 873000, and 1163000 grids for  $H/D$  ratios of 2, 3, and 4, respectively. The results of the mesh independence test for  $H/D = 2$  are presented in Fig. 4.

### 3.4 Reliability Test for Numerical Method

Other similar studies in the literature were reviewed, and the study by Saleha *et al.* (2015) was selected as the reference for the validation of the numerical method and obtained numerical data. For the validation, the analysis was conducted by using the geometry and boundary conditions of the related study. Fig. 5 shows that the results of the present study are consistent with those of Saleha *et al.* (2015).

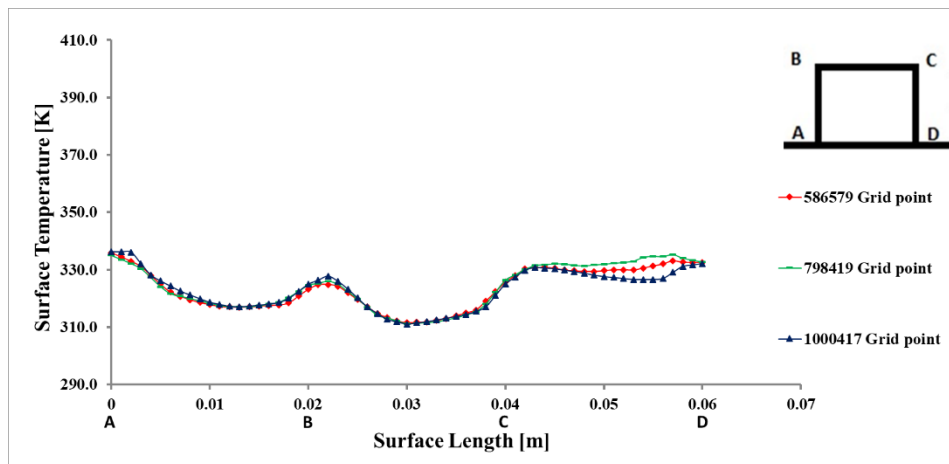


Fig. 4. Comparison of analysis results for different number of grid points when  $H/D = 2$ .

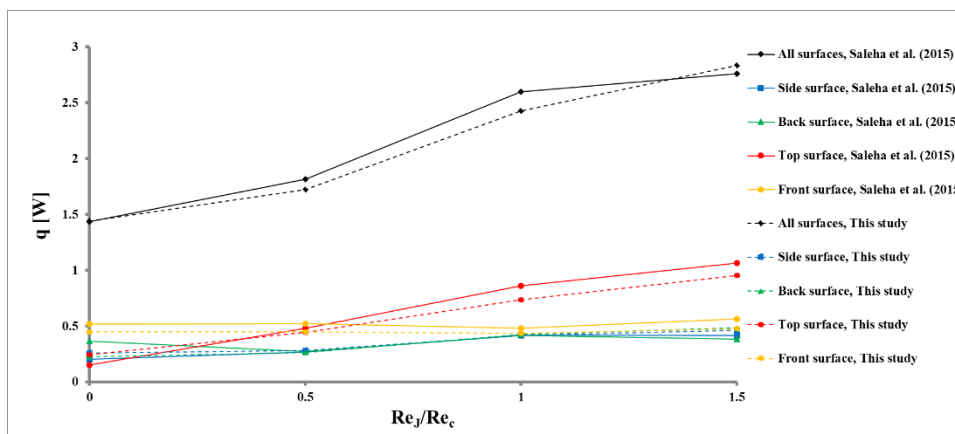


Fig. 5. Comparison of results of the present study with those of Saleha *et al.* (2015).

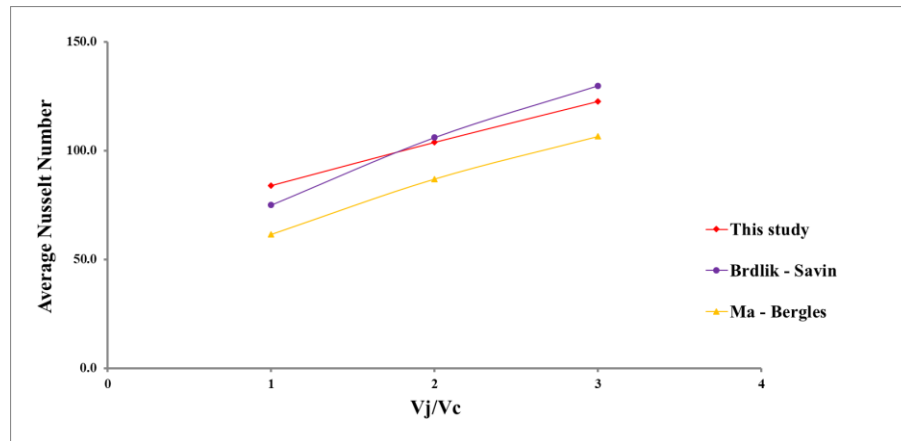


Fig. 6. Comparison of the results of the present study with empirical relations.

### 3.5 Comparison of Numerical Results with Empirical Relations

In addition, the results of the present study were compared with the Brdlik–Savin (Eq. (15)) and Ma–Bergles (Eq. (16)) empirical relations (Obot 1975, Brdlik and Savin 1965, Konecni 1990, Ma and Bergles 1983). The results of this study for hybrid flow and the results from empirical relations for jet flow are shown in Fig. 6. The curve plotted for our study shows trends similar to those for the empirical relations, indicating that the numerical method and results of the present study are reliable.

$$Nu_D = 1.54 Pr^{1/3} Re_D^{0.5} \quad (15)$$

$$Nu_o = 1.29 Pr^{0.4} Re^{0.5} \quad (16)$$

## 4. RESULTS AND DISCUSSION

The study investigated cooling using IJCF for the electronic component under the constant heat flux condition. Accordingly, the analysis was conducted for the four models considering channel Reynolds number of 7778, jet Reynolds numbers of 0, 2916, 5832, and 8748, and  $H/D$  of 2, 3, and 4.

The velocity vector distributions for the different models for  $V_j/V_c=1$  and  $H/D = 3$  are shown in Fig. 7. The figure shows that the general flow structure is similar for all models. The primary fluid moved along the channel from the channel inlet, impinged on the left surface of the electronic component, and flowed over the top surface of the electronic component in all the models. Simultaneously, the secondary flow was directed from the nozzle, impinging on the top surface of the electronic component and repressing the flow of the primary fluid. These primary and secondary flows mixed in the top region of the electronic component and exited the channel by creating a circular flow region on the right-hand side (Fig. 7) of the electronic component.

When the model geometries were analysed separately, the velocity vectors in the top region of the electronic component were denser in Models 2 and 4 than in Models 1 and 3. This is because the flow-guiding fins were present on the left-hand side of Models 2 and 4. The fin narrowed the cross-section, and the primary flow from the channel inlet was directed to the top surface of the electronic component. For Models 3 and 4, with flow-guiding

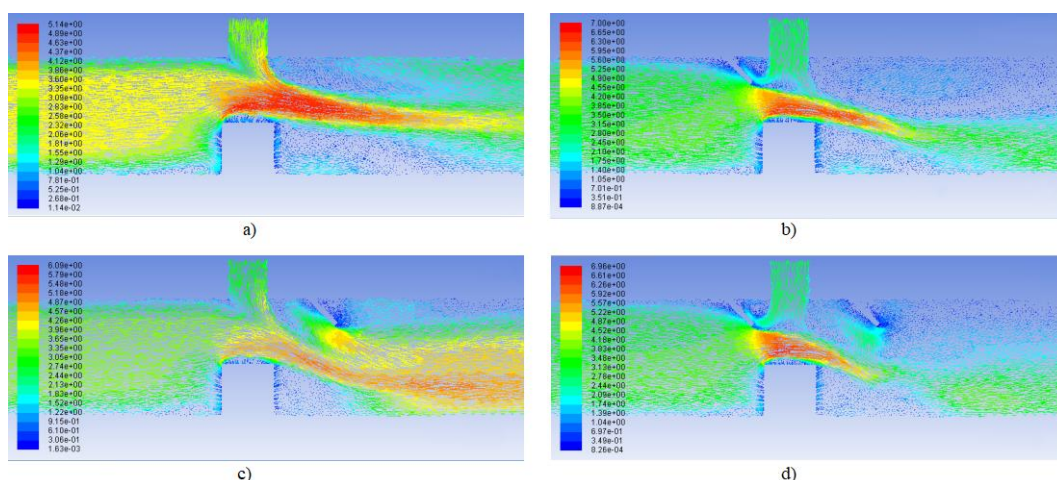
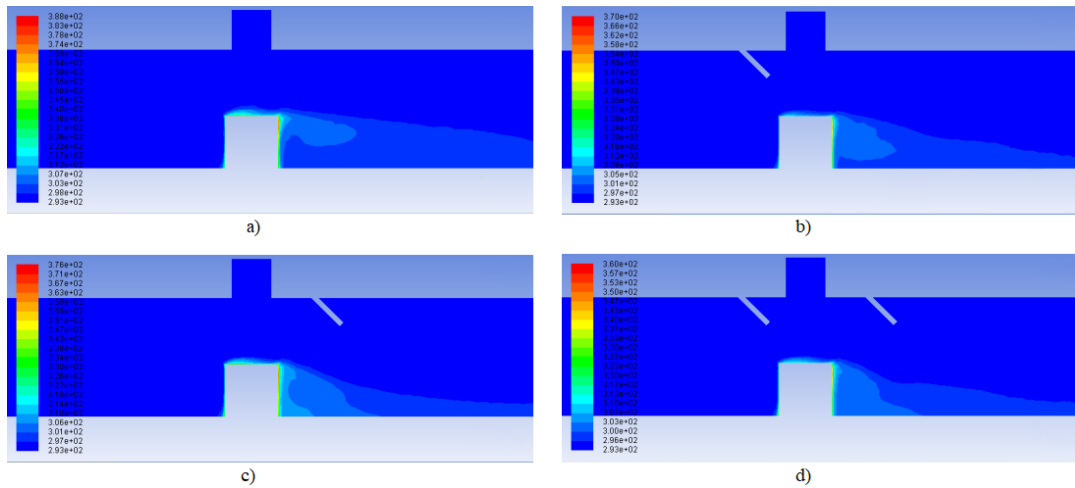


Fig. 7. Velocity vector distribution for different models when  $H/D = 3$  and  $V_j/V_c = 1$ ; a) Model 1, b) Model 2, c) Model 3, and d) Model 4.



**Fig. 8. Temperature distribution for different models when  $H/D = 3$  and  $V_j/V_c = 1$ ; a) Model 1, b) Model 2, c) Model 3, and d) Model 4.**

pins on the right-hand side, the fin directed the flow to the electronic component surfaces on the right-hand side. This decreased the size of the circulation region behind the electronic component (right-hand side in Fig. 7).

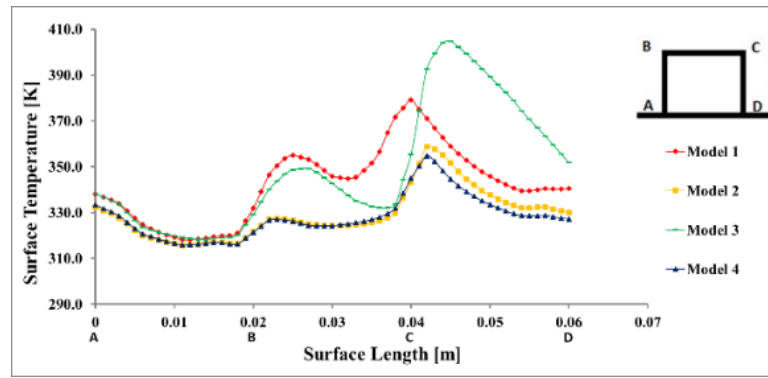
The temperature distributions for the different models for  $V_j/V_c = 1$  and  $H/D = 3$  are shown in Fig. 8. The temperature distributions for all the models are similar. The primary fluid from the channel inlet impinged on the left surface of the electronic component and disrupted the thermal boundary layer on the surface. The primary cross-flow and secondary jet-flow mixed in the top region of the electronic component and increased the convection heat transfer at the top surface. This decreased the top surface temperature of the electronic component. The thermal boundary layer thicknesses in Models 2 and 4 with flow-guiding fins on the left-hand side were thinner than those in the other models. The lowest surface temperatures were observed for Models 2 and 4 with flow-guiding fins on the left-hand side of the electronic component.

Figure 9 presents the variation in the surface temperature with the surface length at the centre plane in the width direction of the channel for different model geometries when the  $H/D$  ratio is 3. Figure 9 a)–d) considers different  $V_j/V_c$  ratios. The highest surface temperature values for all the models were observed for  $V_j/V_c = 0$ . In general, with an increase in the jet inlet velocity, the electronic component surface temperature decreased, and the curves corresponding to the different models were closer. This could be explained by the dominance of secondary jet flow over the cross-flow and the increased forced convection heat transfer from the electronic component. Thus, for low  $V_j/V_c$  ratios, the effect of the model geometry on heat transfer was less significant.

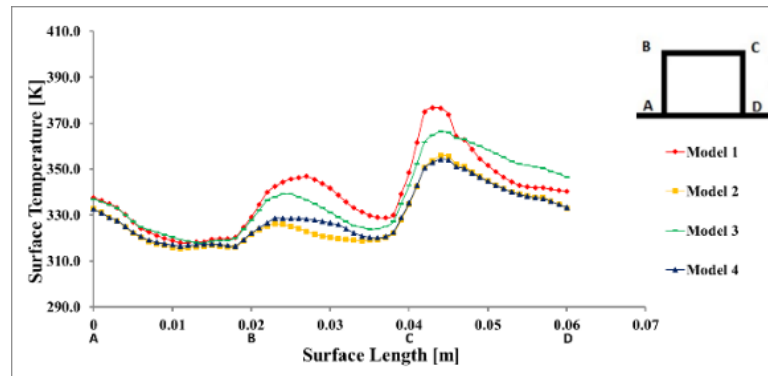
From Fig. 9, for a constant  $V_j/V_c$  ratio, the left-hand side surface temperature of the electronic component

had similar values in all the models. However, the temperatures at the surfaces at the top and right-hand side of the electronic component are different for the different models. The highest temperature values at the top surface were observed for the Model 1 geometry. Model 1 had the basic geometry without fin. With the addition of fins to the geometry, the heat transfer increased, and the top surface temperature decreased. For the surface on the right-hand side of the electronic component, the temperature was the highest in Model 3. In Model 2, the temperatures for all the surfaces of the electronic components were lower than those in the other models. The temperature marginally increased at the surface at the right-hand side of the electronic component in Model 3. Model 4, which combined the fin arrangement in Models 2 and 3, provided the lowest temperatures for the different  $V_j/V_c$  ratios. However, as the  $V_j/V_c$  ratio increased, the effect of the right fin was insignificant, and the highest heat transfer was observed in Model 2.

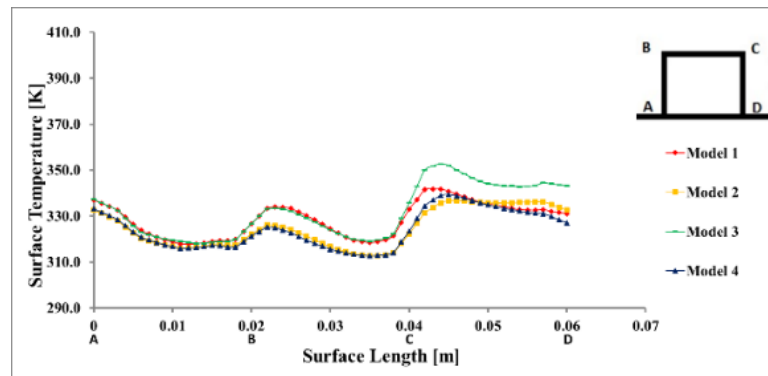
Figure 10 shows the variation in the surface Nusselt number with the surface length at the centre plane in the width direction of the channel for different models and different  $V_j/V_c$  ratios when the  $H/D$  ratio was 3. The maximum Nusselt numbers were obtained for Models 2 and 3. For all the  $V_j/V_c$  ratios, the Nusselt number curves for these two models were higher (higher Nusselt number values) than those of the other models. The common feature of these two models was the presence of a flow-guiding fin on the left-hand side of the electronic component. Thus, adding a flow-guiding fin to the left-hand side improved the Nusselt number. Although the curves for Models 1 and 3 were similar, the Nusselt number values were lower than those of the other models. Model 1 had the basic geometry without fins. Model 3 has a fin on the right-hand side of the electronic component. Thus, adding a flow-guiding fin to the right-hand side of the electronic component had a negligible effect on heat transfer.



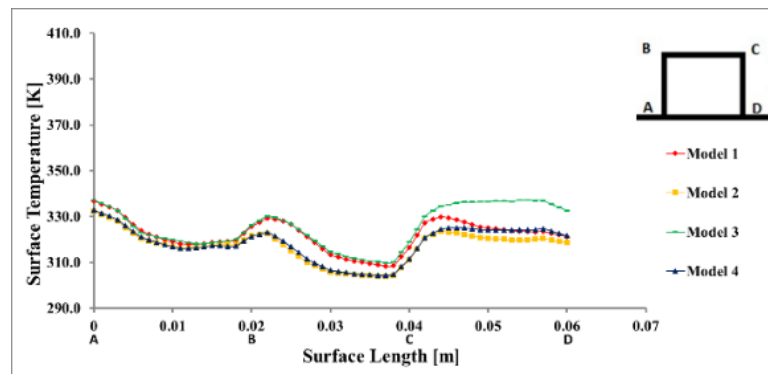
a)  $V_j/V_c = 0$



b)  $V_j/V_c = 1$

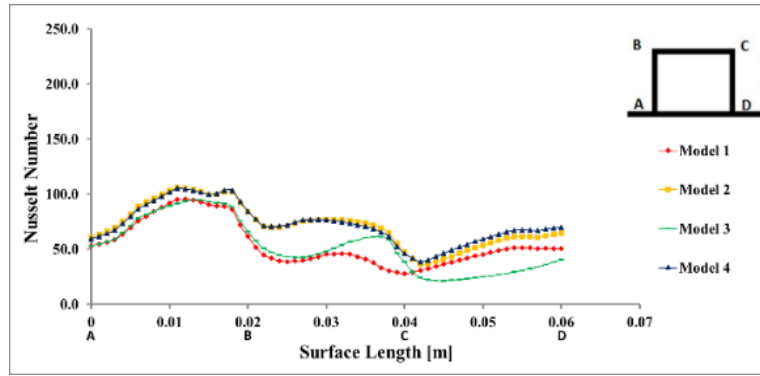


c)  $V_j/V_c = 2$

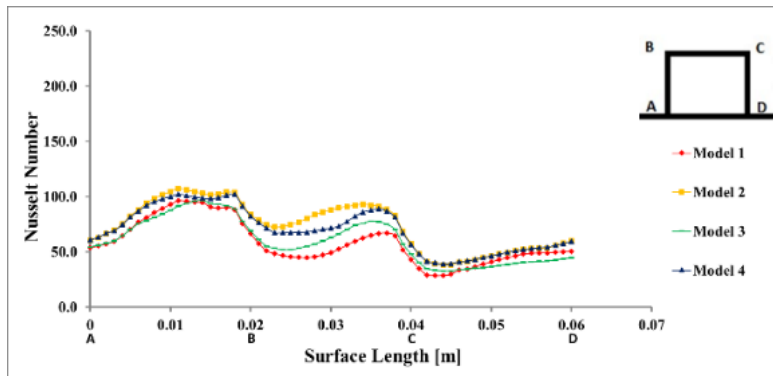


d)  $V_j/V_c = 3$

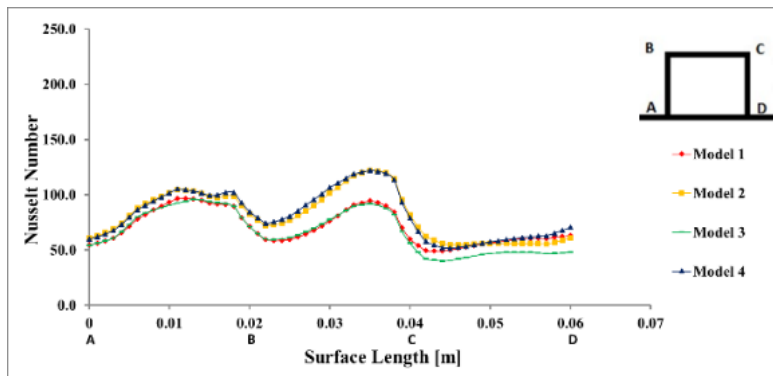
Fig. 9. Variation in the electronic component surface temperature along the surface length for  $H/D = 3$  and different  $V_j/V_c$  ratios.



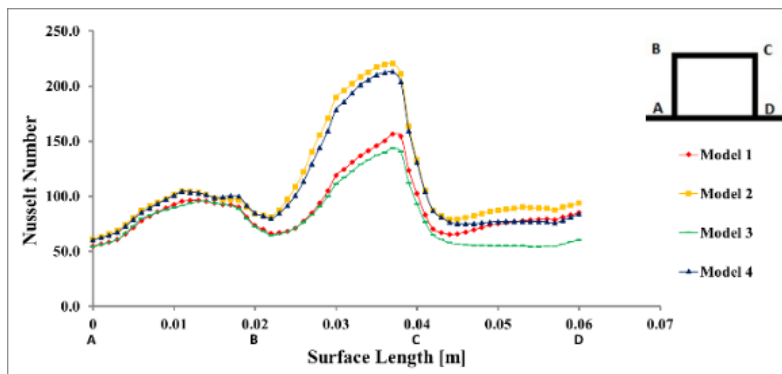
a)  $V_j/V_c = 0$



b)  $V_j/V_c = 1$



c)  $V_j/V_c = 2$



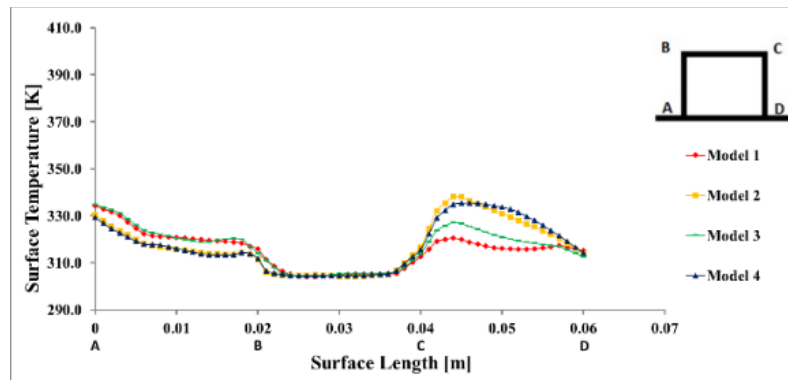
d)  $V_j/V_c = 3$

Fig. 10. Variation in the electronic component surface Nusselt number with the surface length for  $H/D = 3$  and different  $V_j/V_c$  ratios.

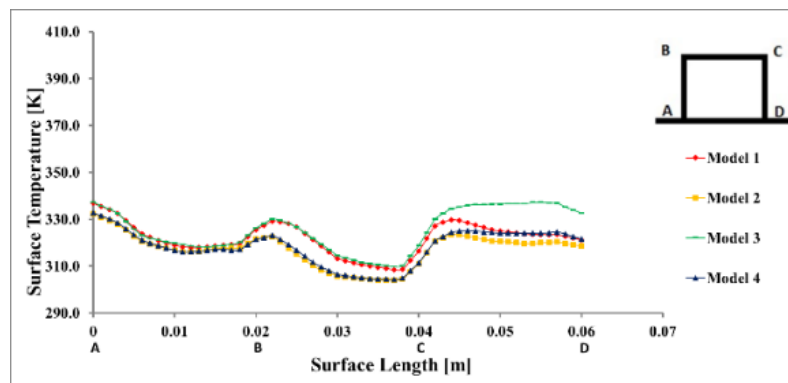
From Fig. 10, an increase in  $V_j/V_c$  ratio increased the Nusselt number. For the  $V_j/V_c$  ratio of 3, the highest Nusselt number was observed on the top surface of the electronic component. This resulted from the increased forced convection on the top surface of the electronic component with the increased secondary jet flow velocity.

Figure 11 shows the variation in the electronic component surface temperature with the surface length at the centre plane in the width direction of the

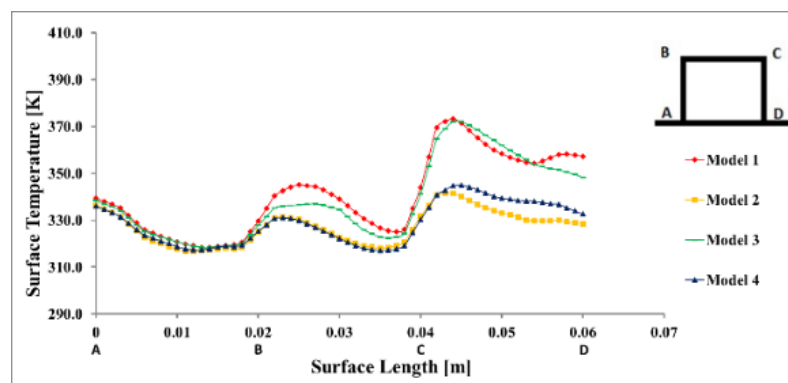
channel for different models and  $H/D$  ratios when the  $V_j/V_c$  ratio is 3. An increase in the  $H/D$  ratio generally increased the electronic component surface level in all the models. The surface temperatures for low  $H/D$  ratios were similar. However, as the  $H/D$  ratio increased, the temperatures of the surfaces at the top and left-hand side of the electronic components in Models 2 and 4 decreased. Thus, adding a flow-guiding fin to the left-hand side in models with a high  $H/D$  ratio enhanced the heat transfer.



a)  $H/D = 2$

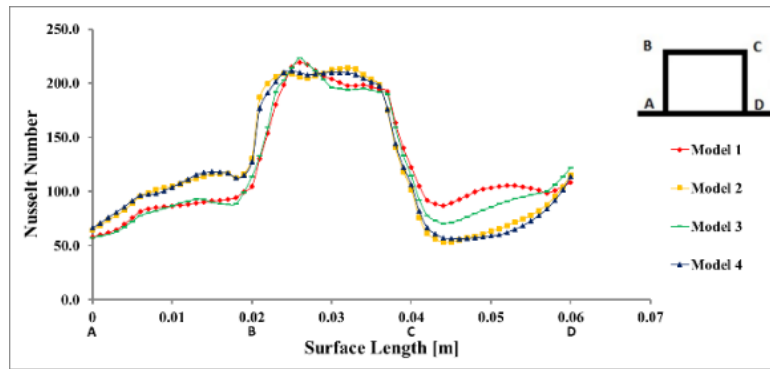


b)  $H/D = 3$

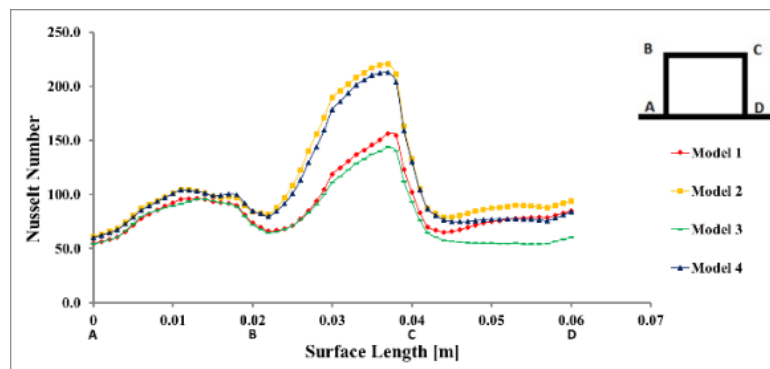


c)  $H/D = 4$

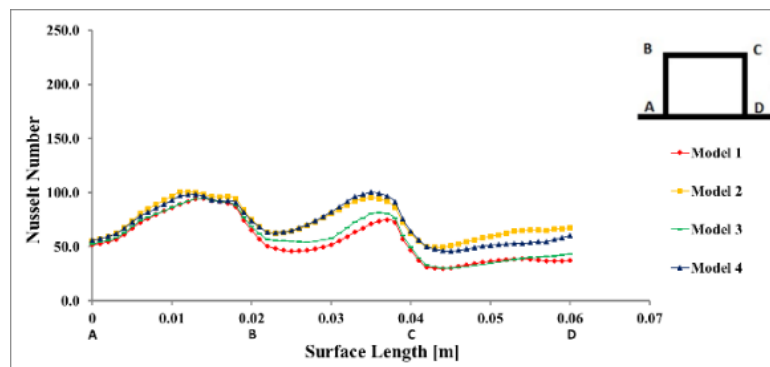
**Fig. 11.** Variation in the electronic component surface temperature with the surface length for  $V_j/V_c = 3$  and different  $H/D$  ratios.



a)  $H/D = 2$



b)  $H/D = 3$



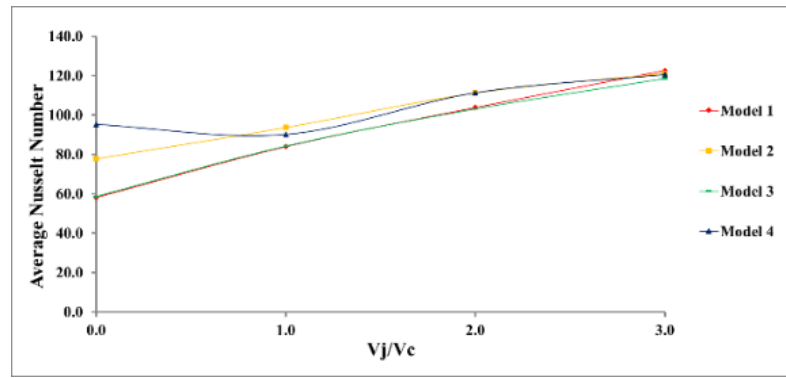
c)  $H/D = 4$

**Fig. 12. Variation in the electronic component surface Nusselt number with the surface length for  $V_j/V_c = 3$  and different  $H/D$  ratios.**

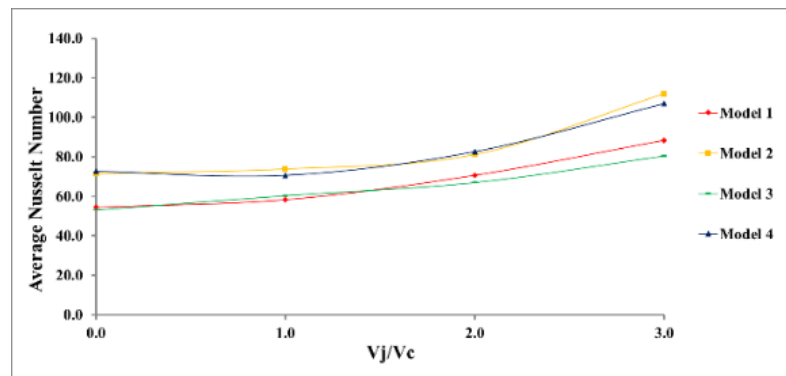
Figure 12 shows the variation in the electronic component surface Nusselt number with the surface length at the centre plane in the width direction of the channel for different models and  $H/D$  ratios when the  $V_j/V_c$  ratio is 3. An increase in the  $H/D$  ratio decreased the maximum Nusselt number in all models. For high  $H/D$  ratios, the maximum Nusselt number for Models 2 and 4 was at the top surface of the electronic component. For all  $H/D$  ratios, the Nusselt number curves for Models 1 and 3 were similar, and those for Models 2 and 4 were similar. The Nusselt numbers obtained for Models 2 and 4 were higher than those of the other models. These two models had fins on the left-hand side of the electronic component. Thus, adding a flow-guiding fin to the left-hand side of the component enhanced the heat transfer. Adding a flow-guiding fin to the

right-hand side of the component had a negligible effect on heat transfer.

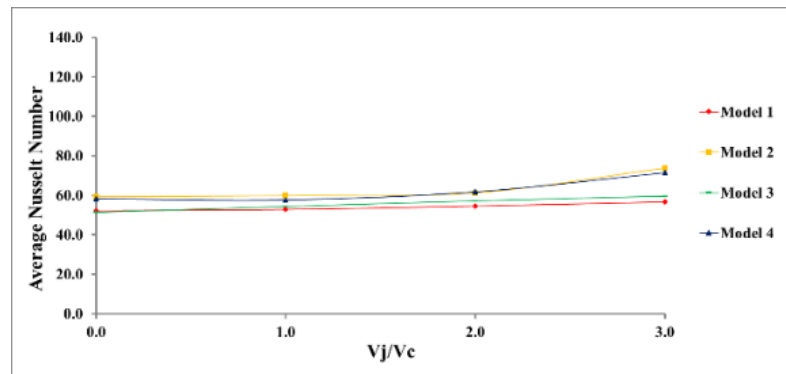
Figure 13 shows the variation in the Nusselt number with  $V_j/V_c$  ratio for different model geometries. An increase in the  $V_j/V_c$  ratio for all the model geometries increased the average Nusselt number. The trend is similar for all the  $H/D$  ratios. In addition, as the  $H/D$  ratio increased, the average Nusselt number decreased. The Nusselt number curves for Models 2 and 4 were similar, and those for Models 1 and 3 were also similar. The average Nusselt number values for Models 2 and 4 were higher than those for the other models. Thus, adding a fin to the left-hand side of the electronic component enhanced the average heat transfer from all the electronic component surfaces.



a)  $H/D = 2$



b)  $H/D = 3$



c)  $H/D = 4$

**Fig. 13. Variation in the average Nusselt number with  $V_j/V_c$  ratio for different model geometries; a)  $H/D = 2$ , b)  $H/D = 3$ , and c)  $H/D = 4$ .**

For  $H/D = 3$ , the variation in pressure losses with  $V_j/V_c$  ratios is given in Fig. 14 for different model geometries. The dominance of secondary jet flow over the primary cross-flow increased with an increase in the  $V_j/V_c$  ratio. The jet flow imposes a resistance on the cross-flow. This leads to increased pressure loss between the channel inlet and outlet. When the effect of the models on the pressure loss was analysed, the highest pressure loss occurred for the models with the fin. The fins increased the velocity of the fluids in the channel and the flow resistance inside the channel. As the flow resistance increased, a higher pressure loss resulted in the models with fins. Similar behaviours were observed for the other  $H/D$  ratios in this study. Among the four

model geometries, the highest pressure loss was observed in Model 4, followed by Models 2, 3, and 1 (in the order of decreasing pressure loss).

The changes in the pressure losses with  $H/D$  ratios for  $V_j/V_c=1$  are shown in Fig. 15 for different model geometries. Fig. 15 indicates that the effect of the jet flow on the combined flow decreased with an increase in the  $H/D$  ratio. Therefore, the cross-flow became more dominant than the jet flow. This led to a decreased resistance created by the jet flow against cross-flow. Therefore, a significant decrease in the pressure difference between the channel inlet and outlet was observed. Similar behaviours were observed for other  $V_j/V_c$  ratios in this study.

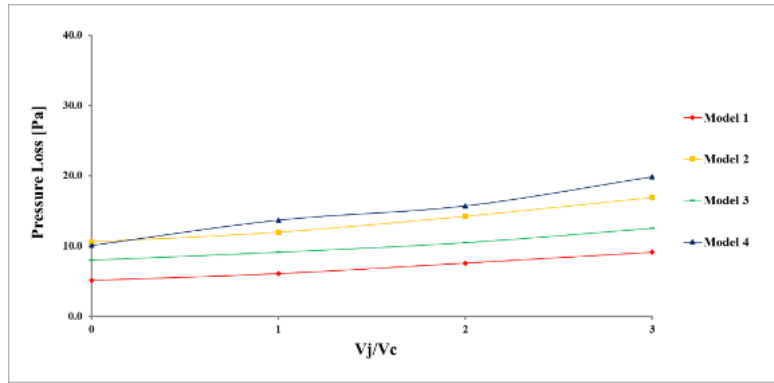


Fig. 14. Variation in the pressure losses with  $V_j/V_c$  ratios for different model geometries for  $H/D = 3$ .

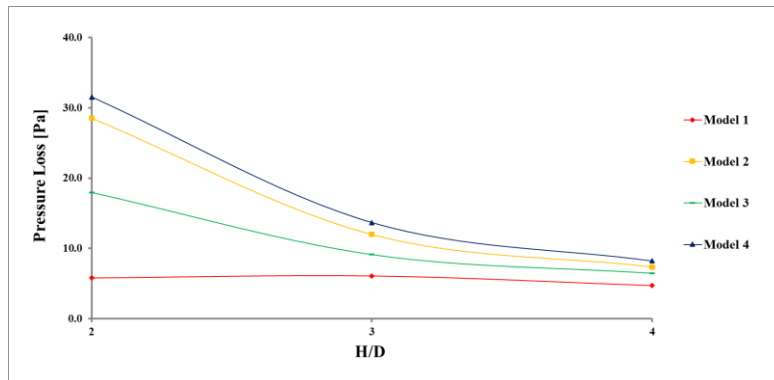


Fig. 15. Variation in pressure losses with  $H/D$  ratio for  $V_j/V_c = 1$  for different model geometries.

## 5. CONCLUSION

This study analysed cooling using an IJCF for an electronic component with constant heat flux. The effects of the change in  $V_j/V_c$  and  $H/D$  on the flow structure, temperature distribution, Nusselt number, and pressure loss were analysed for four different model geometries. As the  $V_j/V_c$  ratio increased, the surface temperatures decreased, and the Nusselt number increased in all models. As the  $H/D$  ratio increased, the surface temperature increased, and the Nusselt number decreased. Therefore, within the analysed parameters, the increased jet inlet velocity and decreased channel height enhanced the heat transfer. The addition of a flow-guiding fin to the model geometry affected the flow structure. Adding a fin to the left-hand side of the electronic improved the heat transfer, whereas adding a fin to the right-hand side of the electronic component had no significant effect on the heat transfer. The addition of fins and increase in the  $V_j/V_c$  ratio increased the pressure loss. An increase in  $H/D$  decreased the pressure loss. For all model geometries, the minimum average Nusselt number value was observed for the highest channel height,  $H/D$  ratio of 4, and  $V_j/V_c = 0$  (absence of jet flow). The maximum value of the Nusselt number was observed for the lowest channel height,  $H/D$  ratio of 2, and highest jet-flow velocity with  $V_j/V_c = 3$ .

## REFERENCES

- Ali, H. M. (2021). Analysis of heat pipe-aided graphene-oxide based nanoparticle-enhanced phase change material heat sink for passive cooling of electronic components. *Journal of Thermal Analysis and Calorimetry* 146, 277–286.
- Arshad, W. and H. M. Ali (2017). Experimental investigation of heat transfer and pressure drop in a straight minichannel heat sink using TiO<sub>2</sub> nanofluid. *International Journal of Heat and Mass Transfer* 110, 248-256.
- Brdlik, P. M. and V. K. Savin (1965). Heat Transfer Between An Axisymmetric Jet And A Plate Normal To The Flow. *Journal of Engineering Physics* 8, 91-98.
- Choo, K., T. Y. Kang and S. J. Kim (2012). The effect of inclination on impinging jets at small nozzle-to-plate spacing. *International Journal of Heat and Mass Transfer* 55, 3327-3334.
- Demircan, T. (2019). Numerical analysis of cooling an electronic circuit component with cross flow and jet combination. *Journal of Mechanics* 35 (3), 395-404.
- Demircan, T. and H. Turkoglu (2010). The Numerical Analysis of Oscillating Rectangular Impinging Jets. *Numerical Heat Transfer, Part*

- A: Applications* 58(2), 146-161.
- Ghaneifar, M., A. Raisi, H. M. Ali and P. Talebizadehsardari (2021). Mixed convection heat transfer of  $Al_2O_3$  nanofluid in a horizontal channel subjected with two heat sources. *Journal of Thermal Analysis and Calorimetry* 143, 2761–2774.
- Guoneng, L., X. Zhihua, Z. Youqu, G. Wenwen and D. Cong (2016). Experimental study on convective heat transfer from a rectangular flat plate by multiple impinging jets in laminar cross flows. *International Journal of Thermal Sciences* 108, 123-131.
- Guoneng, L., Z. Youqu, H. Guilin and Z. Zhiguo (2014). Convective Heat Transfer Enhancement of a Rectangular Flat Plate by an Impinging Jet in Cross Flow. *Chinese Journal of Chemical Engineering* 22(5), 489-495.
- Hadipour, A. and M. R. Zargarabadi (2018). Heat transfer and flow characteristics of impinging jet on a concave surface at small nozzle to surface distances. *Applied Thermal Engineering* 138, 534-541.
- Hatami, M., F. B. Tehrani, A. Abouata and A. M. Ahmar (2018). Investigation of geometry and dimensionless parameters effects on the flow field and heat transfer of impingement synthetic jets. *International Journal of Thermal Sciences* 127, 41-52.
- Incropera, F. P., D. P. Dewit, T. L. Bergman and A. S. Lavine (2007). *Fundamentals of Heat and Mass Transfer (Sixth Edition)*. John Wiley&Sons, Indiana, 447-487.
- Ingoale, S. B. and K. K. Sundaram (2016). Experimental average Nusselt number characteristics with inclined non-confined jet impingement of air for cooling application. *Experimental Thermal and Fluid Science* 77, 124-131.
- Jing, Q., D. Zhang and Y. Xie (2018). Numerical investigations of impingement cooling performance on flat and non-flat targets with dimple/protrusion and triangular rib. *International Journal of Heat and Mass Transfer* 126, 169-190.
- Khan, A., F. Hadi, N. Akram, M. A. Bashir, H. M. Ali, M. M. Janjua, A. Hussain, R. A. Pasha, A. B. Janjua and F. Farukh (2022). Review of micro and mini channels, porous heat sinks with hydrophobic surfaces for single phase fluid flow. *Journal of the Taiwan Institute of Chemical Engineers* 132, 104186.
- Kilic, M. and H. M. Ali (2019). Numerical investigation of combined effect of nanofluids and multiple impinging jets on heat transfer. *Thermal Science* 23 (5B), 3165-3173.
- Konecni, S. (1990). *Flow Measurements And Heat Transfer Studies Of Impinging Jets On Simulated Electronic Packages*. Master's Thesis, Texas University, Arlington.
- Köseoğlu, M. F. (2007). *Experimental and Numerical Investigation of Electronics Equipment Cooling with Impinging Jets*. Ph. D. Thesis, Gazi University Institute of Science and Technology, Ankara.
- Kuraan, A. M., S. I. Moldovan and K. Choo (2017). Heat transfer and hydrodynamics of free water jet impingement at low nozzle-to-plate spacings. *International Journal of Heat and Mass Transfer* 108, 2211-2216.
- Larraona, G. S., A. Rivas, R. Antón, J. C. Ramos, I. Pastor and B. Moshfegh (2013). Computational parametric study of an impinging jet in a cross-flow configuration for electronics cooling applications. *Applied Thermal Engineering* 52, 428-438.
- Ma, C. F. and A. E. Bergles (1983). Boiling Jet Impingement Cooling of Simulated Microelectronic Chips. *Heat Transfer in Electronic Equipment HTD* 28, 5-12.
- Maghrabie, H. M., M. Attalla, H. E. Fawaz and M. Khalil (2017). Numerical investigation of heat transfer and pressure drop of in-line array of heated obstacles cooled by jet impingement in cross-flow. *Alexandria Engineering Journal* 56, 285-296.
- Masip, Y., A. Campo and S. M. Nuñez (2020). Experimental analysis of the thermal performance on electronic cooling by a combination of cross-flow and an impinging air jet. *Applied Thermal Engineering* 167, 114779.
- Masip, Y., A. Rivas, G. S. Larraona, R. Anton, J. C. Ramos and B. Moshfegh (2012). Experimental study of the turbulent flow around a single wall-mounted cube exposed to a cross-flow and an impinging jet. *International Journal of Heat and Fluid Flow* 38, 50-71.
- Mergen, S. (2014). *Numerical investigation of cooling of an electronic component with crossflow and impinging jet*. Master's Thesis, Gazi University Institute of Science and Technology, Ankara.
- Mohammadshahi, S., H. Samsam-Khayani, T. Cai, M. Nili-Ahmadabadi and K. C. Kim (2021). Experimental study on flow characteristics and heat transfer of an oscillating jet in a cross flow. *International Journal of Heat and Mass Transfer* 173, 121208.
- Obot, K. N. (1975). *An Apparatus For Study Of The Effect Of Suction On Heat Transfer For Impinging Round Jets*. Master's Thesis, McGill University, Montreal.
- Örs, E. (2017). *Numerical investigation of cooling of an electronic component with crossflow and impinging jet*. Master's Thesis, Gazi University Institute of Science and Technology, Ankara.
- Ravanji, A. and M. R. Zargarabadi (2020). Effects of elliptical pin-fins on heat transfer characteristics of a single impinging jet on a concave surface. *International Journal of Heat and Mass*

- Transfer* 152, 119532.
- Saleha, N., N. Fadela and A. Abbas (2015). Improving cooling effectiveness by use chamfers on the top of electronic components. *Microelectronics Reliability* 55, 1067-1076.
- San, J. Y. and J. J. Chen (2014). Effects of jet-to-jet spacing and jet height on heat transfer characteristics of an impinging jet array. *International Journal of Heat and Mass Transfer* 71, 8-17.
- Selimefendigil, F. and H. F. Öztop (2014). Pulsating nanofluids jet impingement cooling of a heated horizontal surface. *International Journal of Heat and Mass Transfer* 69, 54-65.
- Sun, B., Y. Qu and D. Yang (2016). Heat transfer of Single Impinging Jet with Cu Nanofluids. *Applied Thermal Engineering* 102, 701-707.
- Wang, C., L. Luo, L. Wang and B. Sundén (2016). Effects of vortex generators on the jet impingement heat transfer at different cross-flow Reynolds numbers. *International Journal of Heat and Mass Transfer* 96, 278-286.
- Wang, C., L. Wang and B. Sundén (2015). A novel control of jet impingement heat transfer in cross-flow by a vortex generator pair. *International Journal of Heat and Mass Transfer* 88, 82-90.
- Wang, C., Z. Wang, L. Wang, L. Luo and B. Sundén (2019). Experimental study of fluid flow and heat transfer of jet impingement in cross-flow with a vortex generator pair. *International Journal of Heat and Mass Transfer* 135, 935-949.
- Wongchareea, K., V. Chuwattanakul and S. Eiamsa-ard (2017). Influence of CuO/water nanofluid concentration and swirling flow on jet impingement cooling. *International Communications in Heat and Mass Transfer* 88, 277-283.
- Xiao, Y., H. Tang, D. Liang and J. Zhang (2011). Numerical study of hydrodynamics of multiple tandem jets in cross flow. *Journal of Hydrodynamics, Ser. B* 23 (6), 806-813.
- Yu, P., K. Zhu, Q. Shi, N. I. Yuan and J. Ding (2017). Transient heat transfer characteristics of small jet impingement on high-temperature flat plate. *International Journal of Heat and Mass Transfer* 114, 981-991.
- Zhong, L., C. Zhou, Z. Sun and S. Chen (2019). Heat transfer mechanisms of inclined jets in cross flow with different holes. *International Journal of Heat and Mass Transfer* 131, 664-674.
- Zhu, K., P. Yu, N. Yuan and J. Ding (2018). Transient heat transfer characteristics of array-jet impingement on high-temperature flat plate at low jet-to-plate distances. *International Journal of Heat and Mass Transfer* 127, 413-425.
- Zuckerman, N. and N. Lior (2006). Jet impingement heat transfer: Physics, correlations, and numerical modeling. *Advances in Heat Transfer* 39, 565-631.